

SCIENTIFIC REPORTS



OPEN

Rough gold films as broadband absorbers for plasmonic enhancement of TiO₂ photocurrent over 400–800 nm

Received: 06 April 2016

Accepted: 29 June 2016

Published: 09 September 2016

Furui Tan^{1,2}, Tenghao Li¹, Ning Wang^{1,2}, Sin Ki Lai¹, Chi Chung Tsoi¹, Weixing Yu³ & Xuming Zhang^{1,2}

Recent years have witnessed an increasing interest in highly-efficient absorbers of visible light for the conversion of solar energy into electrochemical energy. This study presents a TiO₂-Au bilayer that consists of a rough Au film under a TiO₂ film, which aims to enhance the photocurrent of TiO₂ over the whole visible region and may be the first attempt to use rough Au films to sensitize TiO₂. Experiments show that the bilayer structure gives the optimal optical and photoelectrochemical performance when the TiO₂ layer is 30 nm thick and the Au film is 100 nm, measuring the absorption 80–90% over 400–800 nm and the photocurrent intensity of 15 $\mu\text{A}\cdot\text{cm}^{-2}$, much better than those of the TiO₂-AuNP hybrid (i.e., Au nanoparticle covered by the TiO₂ film) and the bare TiO₂ film. The superior properties of the TiO₂-Au bilayer can be attributed to the rough Au film as the plasmonic visible-light sensitizer and the photoactive TiO₂ film as the electron acceptor. As the Au film is fully covered by the TiO₂ film, the TiO₂-Au bilayer avoids the photocorrosion and leakage of Au materials and is expected to be stable for long-term operation, making it an excellent photoelectrode for the conversion of solar energy into electrochemical energy in the applications of water splitting, photocatalysis and photosynthesis.

TiO₂ has been extensively investigated as a photoelectrode for various applications, including photoelectrochemical water splitting^{1,2}, pollutant degradation^{3,4}, *et al.*, thanks to its excellent chemical stability, photocorrosion resistance and low cost. As an n-type semiconductor with a wide band gap around 3.2 eV, it can only absorb UV light (cutoff wavelength \sim 388 nm), causing a low utilization efficiency of solar light that spans from UV to infrared region. Therefore, an ideal photoelectrode for the solar photocatalysis should have a broadband absorption in the wavelength range of 400–800 nm. For practical applications, the photoelectrode should be stable, low cost and easy fabrication of large-area samples. In the past decade, plasmonic metal nanoparticles (NPs) have been widely used to sensitize the host semiconductor TiO₂ to visible light^{5,6}. However, most studies rely on the metal NPs with uniform shape and size to obtain visible light response, whose absorption due to the localized surface plasmon resonance (LSPR) is often limited to a narrow spectral range^{7,8}. Since the broad absorption band can be regarded as a combination of many absorption peaks, Au NPs with different sizes and/or shapes may be used, but this is not favorable due to the fabrication complexity. Additionally, multiple resonant peaks could also be obtained by use of the multipolar resonances in different directions^{9,10}, but the processing techniques appear to be complicated^{11–13}. To address this problem, broadband resonant nanostructures with simple fabrication are highly desired.

Here we present an original design of plasmonic strong absorber for solar energy harvesting and photocatalysis application in the visible region. This absorber, the TiO₂-Au bilayer, consists of two simple layers, a rough Au film at the bottom as the plasmonic antenna to absorb optical energy for photo-excited electron generation and a TiO₂ film at the top as the photocatalyst to receive the electrons for the photocurrent transfer. Simple processes like the magnetic sputtering and the thermal annealing are adopted to fabricate the rough Au film, which is equivalent to a collection of random Au nanostructures with different geometries and sizes. Consequentially, this TiO₂-Au bilayer supports the plasmon resonance of individual nanostructures and the plasmonic coupling of

¹Department of Applied Physics, The Hong Kong Polytechnic University, Hong Kong, P. R. China. ²The Hong Kong Polytechnic University Shenzhen Research Institute, Shenzhen, P. R. China. ³Key Laboratory of Spectral Imaging Technology, Xi'an Institute of Optics and Precision Mechanics, Chinese Academy of Sciences, Xi'an, P. R. China. Correspondence and requests for materials should be addressed to X.Z. (email: apzhang@polyu.edu.hk)

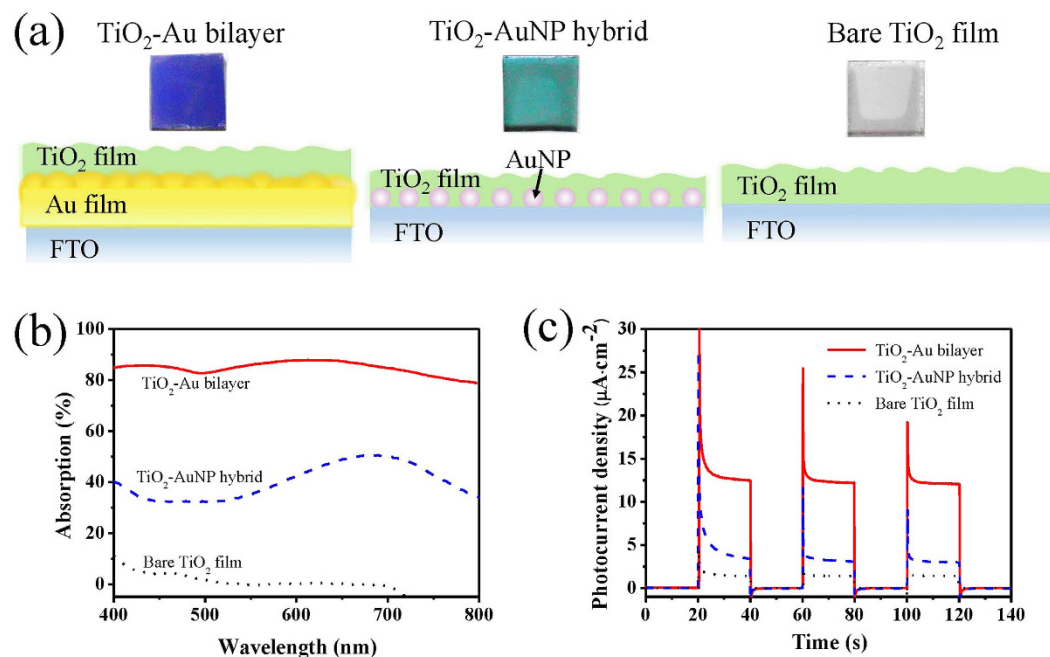


Figure 1. (a) Photographs and schematic diagrams of the three samples, from left to right, the TiO₂-Au bilayer, the TiO₂-AuNP hybrid and the bare TiO₂ film, each sample has the footprint of 1 cm × 1 cm; (b) the absorption spectra and (c) *I-t* plots of the TiO₂-Au bilayer (red solid lines), the TiO₂-AuNP hybrid (blue dashed lines) and the bare TiO₂ film (black dotted lines), respectively. The TiO₂ films of the three samples are all 30 nm thick. The bias potential for the *I-t* measurement is 0 V vs SCE (i.e., saturated calomel electrode).

neighboring nanostructures, and enables the broadband absorption in the visible wavelength range from 400 to 800 nm, acting effectively as a broadband visible-light absorber. This kind of visible-light absorbers have already been used in photothermal systems that rely on the heat^{10,14}, but their great potential for the photocurrent generation has been merely overlooked. The photoelectrochemical performance of the TiO₂-Au bilayer demonstrates apparent enhancement as compared to the TiO₂-AuNP hybrid (i.e., Au NPs covered by TiO₂ film) and the bare TiO₂ film, indicating superior ability of electron generation and transfer. We further examine the influence of the thickness of TiO₂ film on the properties of the TiO₂-Au bilayer, and find that the optimal thickness is 30 nm. The fabrication techniques of the TiO₂-Au bilayer are relatively simple and cost-effective. Additionally, in contrast to the previously reported AuNP-TiO₂ systems (i.e., Au NPs on top of the TiO₂ film)¹⁵⁻¹⁷, the TiO₂-Au bilayer buries the Au film under the TiO₂ film and thus protects the Au film from the photocorrosion and leakage during the photochemical reactions, making it promising for long-term operation.

Results

Comparison of TiO₂-Au bilayer, TiO₂-AuNP hybrid and bare TiO₂ film. Figure 1a shows the photos and the schematic diagrams of the proposed structures, including the TiO₂-Au bilayer, the TiO₂-AuNP hybrid and the bare TiO₂ film. For the bare Au film deposited on the FTO glass, it appears dark yellow. After this bare Au film is covered by the 30-nm TiO₂ film to form the TiO₂-Au bilayer, it turns to dark blue after the annealing treatment (see the left of Fig. 1a). The characteristic color of Au NPs is pinkish, which turns into jade color after the coverage of the 30-nm-thick TiO₂ film to form the TiO₂-AuNP hybrid (see the middle of Fig. 1a). The bare TiO₂ film exhibits a light gray color (see the right of Fig. 1a). It is noted that the edge parts of samples have slightly different colors from the central parts, because the central parts have TiO₂ deposited only on one side, whereas the edge parts are covered on both sides due to some process details. One-sided TiO₂ deposition is favorable for optical spectrum measurements as compared to two-sided TiO₂ deposition since the latter may result in a non-uniform film on the back side. In experiments, only the central parts with a diameter of 1 mm is used to investigate the photoelectrochemical properties¹⁸.

A key step to improving the photocurrent is to increase the optical absorption in visible range. Figure 1b compares the absorption spectra of the TiO₂-Au bilayer, the TiO₂-AuNP hybrid and the bare TiO₂ film. Here the absorption *A* is calculated by the equation $A = 1 - R - T$, where *R* and *T* are the normalized reflection and transmission, respectively, as shown in Fig. S2a,b. The bare TiO₂ film shows high reflection and transmission over 400–800 nm, resulting in very weak absorption (see Fig. 1b). The TiO₂-AuNP hybrid shows obvious enhancement of absorption, especially near 680 nm, which can be attributed to the LSPR effect of the Au NPs. In contrast, the TiO₂-Au bilayer exhibits much stronger absorption. Particularly, the absorption spectrum is flat over the whole range of 400–800 nm, with the minimum absorption of 80% and the maximum 90%.

The light-harvesting capability plays an important role for the enhanced photoelectrochemical activity under the visible light irradiation. The photoactivities of these three TiO₂-based samples are evaluated using the *I-t*

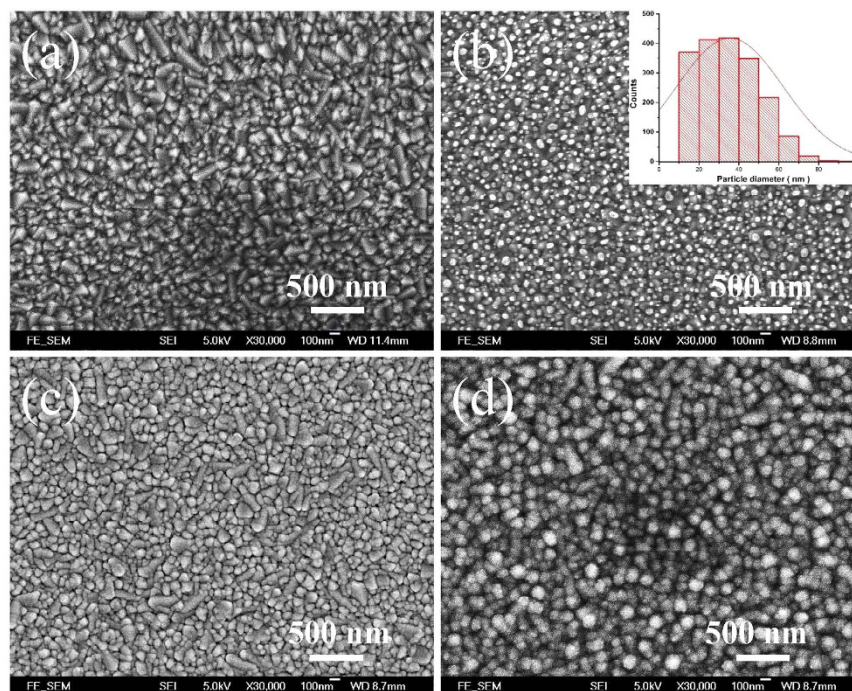


Figure 2. Scanning electron micrographs of the surface morphologies of different layers of the samples. (a) FTO glass; (b) Au NPs on FTO glass, deposited by the sputtering process; (c) rough Au film on FTO glass; (d) ALD-deposited TiO₂ film on the rough Au film. The inset in (b) is the histogram of the size of Au NPs.

technique. Figure 1c plots the curves of photocurrent density at the 0-V bias potential. The transient photocurrent responses of the three TiO₂-based samples are measured for several on-off cycles of irradiation. The rise and fall of the photocurrent respond well to the switching on and off of the visible-light irradiation (wavelength >400 nm). The photocurrent drops to zero as soon as the irradiation is turned off, and recovers immediately when the irradiation is turned on again. It indicates that the current is completely due to the visible-light response of the photoelectrode, and the charge transport is very fast. As can be read from Fig. 1c, the TiO₂-Au bilayer produces the transient photocurrent density of 12.4 $\mu\text{A}\cdot\text{cm}^{-2}$, higher than the TiO₂-AuNP hybrid (3.2 $\mu\text{A}\cdot\text{cm}^{-2}$) and the bare TiO₂ film (1.5 $\mu\text{A}\cdot\text{cm}^{-2}$) by a factor of 3.8 and 8.2. This indicates that the TiO₂-Au bilayer has the best effect on charge generation, separation and transport¹⁹. In addition, the order of the photocurrent densities agrees with the absorption measurements in Fig. 1b. As a supplement, the *I-t* plots of the TiO₂-AuNP hybrid and the bare TiO₂ film are shown in Fig. S3(c,d), under monochromatic lights at the wavelengths of 420, 450, 475, 500, 520, 550, 600 and 650 nm, respectively. For quantitative comparison, the action spectra (i.e., photocurrent density versus light wavelength) are plotted in Fig. S3e for the three samples. It is seen that the TiO₂-Au bilayer has the highest response under every monochromatic light illumination, showing significant enhancement by a factor of about 2 as compared to the TiO₂-AuNP hybrid and the bare TiO₂ film.

For the TiO₂-Au bilayer and the TiO₂-AuNP hybrid, their differences in *I-t* plot and action spectrum can be explained below. From the physical mechanisms, the enhancement of photocurrent in the TiO₂-Au bilayer and the TiO₂-AuNP hybrid should be attributed to the Au nanostructures and the formation of Schottky junctions at the interfaces of Au and TiO₂. The former enables the optical absorption to visible light, whereas the latter improves the separation of photo-generated electron-hole pairs and suppresses the recombination of photogenerated charge. But there are still some differences between the TiO₂-Au bilayer and the TiO₂-AuNP hybrid, lying in mostly the density of Au nanostructures. In the TiO₂-Au bilayer, the rough Au film can be regarded as an assembly of densely-packed random Au nanostructures (e.g., NPs, nanocavities) with different shapes and sizes (see detailed discussion below). The dense packing results in a large number of Au nanostructures, and the LSPR effect of every single Au nanostructure sums up to high absorption over a wide span of wavelength; moreover, the dense packing enables the plasmonic coupling of neighboring Au nanostructures and further enhances the optical absorption. In addition, the dense packing provides good electrical connections among the Au nanostructures for the transport and distribution of photogenerated charges. Furthermore, the rough Au film provides large interface area between the Au and TiO₂ for the Schottky junction and enables the efficient transfer of photo-excited electrons and holes between Au to TiO₂. In comparison, the TiO₂-AuNP hybrid has relatively low density of Au NPs, causing not that ideal absorption and charge transfer. As a result, the TiO₂-Au bilayer has stronger absorption than the TiO₂-AuNP hybrid and is expected to have larger photocurrent.

Figure 2 displays the surface morphologies of the respective layers of the three types of TiO₂-based samples. The surface of FTO glass itself is already very rough as shown in Fig. 2a. For the Au NPs on the FTO glass, the deposited thin Au film with a thickness around 8 nm is transformed to discontinuous Au NPs after the annealing as shown in Fig. 2b^{20,21}. When viewed from the top, the Au NPs exhibit nearly round shape and similar particle

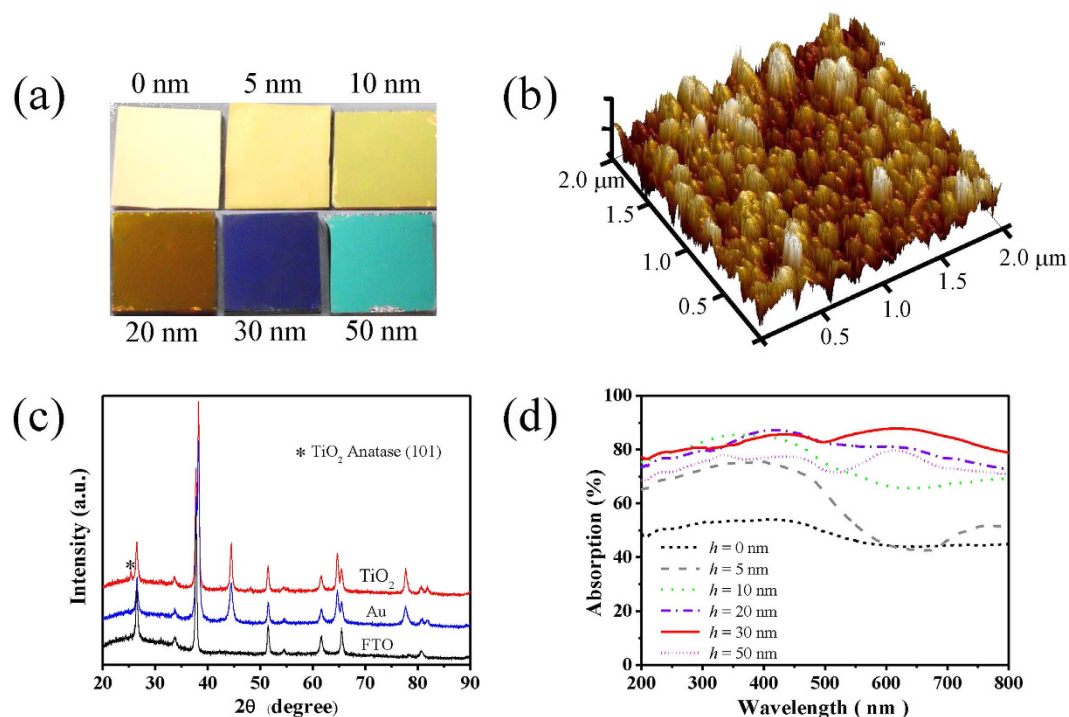


Figure 3. (a) Photographs of the TiO₂-Au bilayer samples with the TiO₂ thicknesses of 0, 5, 10, 20, 30 and 50 nm. The films are deposited by the ALD at 100 °C and then annealed at 500 °C for 1 h; (b) atomic force micrograph of the surface morphology of the rough Au film on the FTO substrate; (c) the XRD patterns of the bare TiO₂ film, the bare Au film and the FTO substrate; and (d) the absorption spectra of different TiO₂-Au bilayer samples.

size. The histogram of the particle size distribution is obtained with the free software ImageJ as shown in the inset of Fig. 2b. The Au NPs have an average size of 35 nm with a standard deviation of approximately 11 nm. When the thickness of the deposited Au film is increased to 100 nm, the surface of Au film becomes rough and thus a pattern of densely packed metallic cluster grows up, which seems like a collection of many Au nanostructures with large variations of shape and size, as shown in Fig. 2c. The TiO₂ film deposited by the atomic layer deposition (ALD) process on the rough Au film has quite uniform grain size of TiO₂ nanoparticles as shown in Fig. 2d. These structural layers in a larger area are shown in Fig. S1.

Influence of TiO₂ film thickness of TiO₂-Au bilayer. The thickness of the TiO₂ film plays an important role in the optical and photoelectrochemical properties of the TiO₂-Au bilayer. To examine this influence, a series of TiO₂ thin film are deposited onto the Au film by the ALD method, including 0, 5, 10, 20, 30 and 50 nm. The ALD is a precision growth technique that can passivate surface states to decrease the surface recombination velocity, which can synthesize thin film from only a few atomic layers to hundreds of nanometers^{22,23}. Its layer-by-layer deposition allows highly conformal coating even on the dense and rough surfaces of nanostructures. Therefore, the as-deposited TiO₂ films with excellent step coverage have amorphous structure. The thickness of TiO₂ film can be controlled by the deposition time according to the deposition condition. Color photographs of the TiO₂-Au bilayer samples with various TiO₂ thicknesses are shown in Fig. 3a. The sample with the 0-nm TiO₂ film represents only the rough Au film, which looks bright yellow. The samples appear deepened yellow when the TiO₂ thickness is increased from 5 to 20 nm. The sample becomes dark blue when the TiO₂ thickness is 30 nm, and turns to jade for the 50-nm TiO₂. The atomic force microscopy (AFM) is also employed to characterize the surface morphology of the rough Au film (Fig. 3b), which agrees well with the measured SEM image (Fig. 2c). The mean roughness of the rough Au film is approximately 5 nm within the area of 2 μm × 2 μm and the root-mean-square (rms) roughness is 15 nm, indicating significant surface roughening. Moreover, the XRD patterns (Fig. 3c) of the TiO₂ films match the Joint Committee on Powder Diffraction Standards File (JCPDS no. 21-1272), which confirms the anatase phase of TiO₂²⁴. It is well known that the anatase phase of TiO₂ has greater photocatalytic activity than the rutile phase due to the lower conduction band and higher hydrophilicity²⁵. For the influence of the Au film thickness, it has little effect as long as the Au film is thick enough to block all the light and rough enough to enable strong, broadband absorption of visible light. Therefore, this study does not investigate the influence of Au film thickness, but simply maintains the Au film thickness at 100 nm, which is much thicker than the skin depth of Au film (about 13 nm). The surface of the 100-nm Au film after annealing is still very rough for plasmonic absorption²⁶.

The absorption spectra of these TiO₂-Au bilayer samples with different TiO₂ thicknesses are also determined by $A = 1 - R - T$ as shown in Fig. 3d. It is seen that the absorption increases with the TiO₂ thickness from 0 to

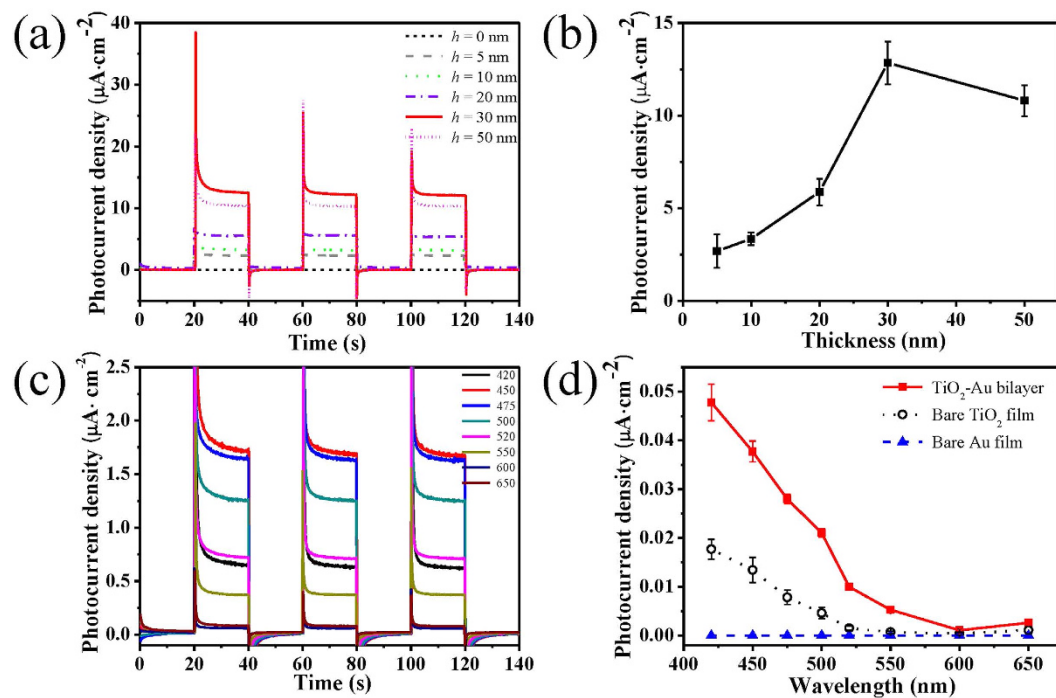


Figure 4. (a) *I-t* plots and (b) photocurrent densities of the TiO₂-Au bilayer samples with the TiO₂ thicknesses of 0, 5, 10, 20, 30 and 50 nm, here the sample of 0 nm represents the rough TiO₂ film itself; (c) *I-t* plots under the irradiation of different monochromatic wavelengths; and (d) action spectra (i.e., photocurrent versus wavelength) of the TiO₂-Au bilayer (red line) and its constituent layers – the bare TiO₂ film (black line) and the bare Au film (blue line), here the TiO₂ film is always 30 nm thick.

30 nm, but starts to decrease when the thickness is over 30 nm. More details of the reflection and transmission spectra are given in Fig. S2 of the Supplementary Information. Figure S2c shows that the reflection first decreases with thicker TiO₂, reaches the minimum at 30 nm and then increases. From Fig. S2d, the transmission shares the similar trend, except that it has two peaks at around 500 nm and 700 nm, though the level of transmission is always <10%.

The results of *I-t* measurements are plotted in Fig. 4a for the TiO₂-Au bilayer samples with different TiO₂ film thicknesses. It is seen that the photocurrents respond immediately and repeatedly to the turning on and off of light source. Figure 4b plots the measured photocurrent density as a function of the TiO₂ thickness, showing the maximum $12.4 \mu\text{A}\cdot\text{cm}^{-2}$ at 30 nm. Therefore, the TiO₂-Au bilayer sample with the 30-nm-thick TiO₂ film has the highest photocurrent, this sample is named as the “optimal bilayer sample”. To further investigate the wavelength dependence, the optimal bilayer sample is illuminated with a broadband visible light source ($\lambda \geq 400$ nm) that delivers a total power of $\sim 300 \text{ mW}/\text{cm}^2$ (see Fig. S3a of Supplementary Information for the calibrated emission spectrum). The light source employs a series of narrow-band optical filters to filter the broadband light into roughly monochromatic light. The source intensity as a function of the wavelength using the optical filters is plotted in Fig. S3b, agreeing with the spectrum of visible light source (see Fig. S3a)²⁷. The *I-t* plots of the optimal bilayer sample are shown in Fig. 4c for the wavelengths of 420, 450, 475, 500, 520, 550, 600 and 650 nm, respectively. As a supplementary, the *I-t* plots of the bare TiO₂ film and the TiO₂-AuNP hybrid are also shown in Fig. S3c,d, respectively. For quantitative comparison, the action spectra (i.e., photocurrent density versus light wavelength) are plotted in Fig. 4d for the optimal bilayer sample and its constituent layers—the 30-nm-thick bare TiO₂ film and the bare Au film. It is seen that the bare Au film has almost no response whereas the optimal bilayer sample has the highest result, showing significant enhancement as compared to the bare TiO₂ film. For the optimal bilayer sample, the photocurrent density drops quickly when the wavelength goes up to 600 nm and becomes very low afterward. The energy conversion efficiencies of the three samples can also be indicated by the incident photon to current efficiency (IPCE), which are extracted from the measured photocurrents and the incident spectrum. The IPCE of the optimal TiO₂-Au bilayer sample reveals a clear enhancement as compared to the bare TiO₂ film and the bare Au film, which is consistent with the action spectra plotted in Fig. 4d.

Simulation. Based on the physical structure and materials of the actual TiO₂-Au bilayer sample, the simulation model is built up as depicted in Fig. 5a, with the Au portion and the TiO₂ portion denoted by yellow and blue color, respectively. The model consists of three layers, from bottom to top, a flat Au film layer, an Au NPs layer and a TiO₂ layer. The FTO thin film is not included in the simulation since there is almost no transmission of light through the Au layer. As an approximation, the thickness of the flat Au film layer is 100 nm in the simulation. Considering the roughness of the Au film (see the AFM image in Fig. 3b), the rough surface is represented by randomly-distributed particles²⁸. In the simulation, the particles are randomly scattered on the surface in a space

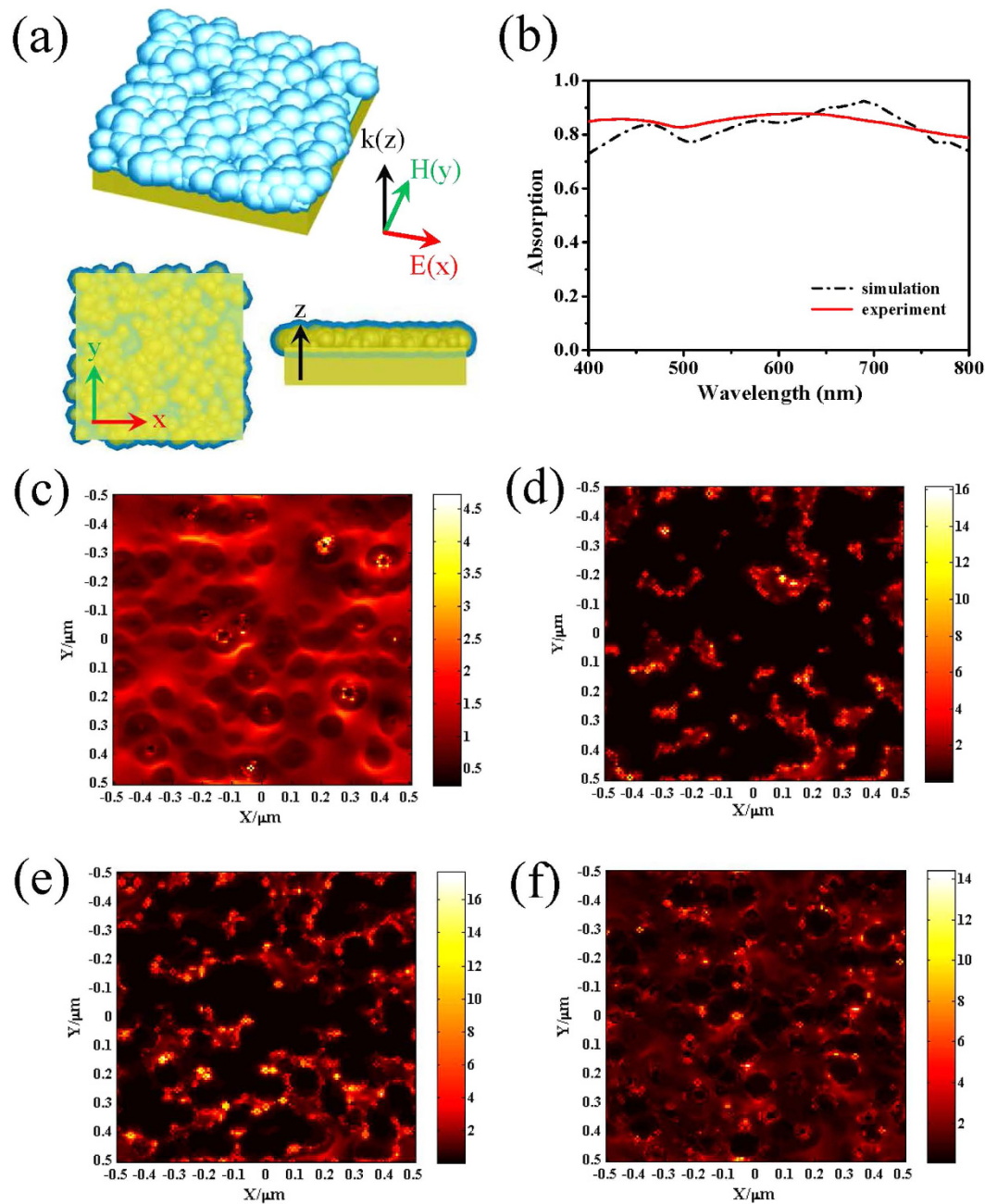


Figure 5. Simulation results. (a) Perspective view, top cross-sectional view (XY plane) and side cross-sectional view (XZ plane) of the model for the TiO_2 -Au bilayer sample; (b) comparison of the measured absorption spectrum with the calculated one using the FDTD method for the TiO_2 -Au bilayer sample whose TiO_2 film is 30-nm thick; The electric field distributions on the transverse cross-sections located at (c) $Z = 0$ nm, (d) $Z = 30$ nm, (e) $Z = 60$ nm and (f) $Z = 90$ nm, here $Z = 0$ is at the upper surface of the flat Au layer.

of $1\ \mu\text{m} \times 1\ \mu\text{m} \times 30\ \text{nm}$, with their diameters varying from 60 to 120 nm. The vertical positions of the particles are adjusted so that the highest particles are always attached to the upper boundary of the flat Au layer while the other particles may be partially embedded into the flat Au layer. The Au nanoparticles can be overlapped with each other, in which some larger domain can be formed occasionally to further account for the randomness of the distribution, the shape and the size. To mimic the TiO_2 film, the template method is adopted²⁹. Each Au NPs is embraced by a shell layer of TiO_2 , whose thickness is equal to the ALD deposition thickness approximately. For the bare area without the Au NPs covered, a flat TiO_2 film layer with the deposition thickness is also added above the flat Au layer. The meshing order of these Au NPs has higher priority than the TiO_2 layers to ensure the coverage by TiO_2 at only the outer boundaries. The transverse dimension of the model structure is $1\ \mu\text{m} \times 1\ \mu\text{m}$ and the number of Au NPs is 320 in the simulation. With the random positioning, the number of Au NPs is essential for

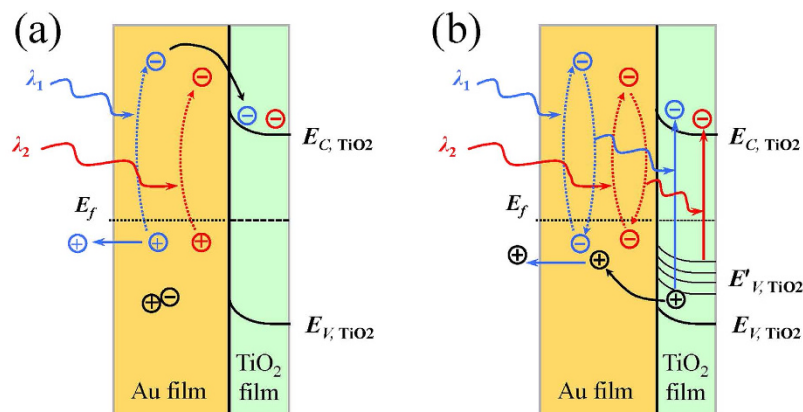


Figure 6. Mechanisms of the photocurrent generation in the TiO₂-Au bilayer. (a) Hot electron injection, for which the rough Au film absorbs photons of different wavelengths to generate hot electrons, whose potential levels of excited states are high enough to overcome the potential barrier to be injected into the TiO₂ layer. (b) Plasmonic resonance energy transfer, for which the plasmonic resonance of Au nanostructures generates intense electric fields in the TiO₂ layer and excites the electrons of TiO₂ to the conduction band. For the energy's point of view, the photon energy excites the Au electrons, which falls back and transfers the energy to the TiO₂ electrons via the intense electric field near the plasmonic hot spots.

simulating the surface roughness of the Au film, and a relatively small number generally implies a larger surface roughness. In this way, the roughness of Au surface of the real TiO₂-Au bilayer can be well represented.

Regarding the boundary condition, Perfectly Matched Layer (PML) is used for both the top and bottom boundaries, while periodic condition is employed for the other side boundaries. The periodic condition is a good approximation as the model's transverse dimension is large as compared to the particle size to support the randomness of distribution. The 4th level auto non-uniform meshing is applied to balance the simulation accuracy and the computation load. The S parameter analysis group is implemented for the absorption analysis, in which a plane source is used and the far-field measurement is conducted. In the simulations, the average thickness of the TiO₂ layer is varied from 5 to 50 nm. The absorption spectrum of the absorber is recorded for each thickness, within the wavelength range of 400–800 nm.

The simulated absorption spectrum (black line) for the TiO₂-Au bilayer sample with the 30-nm TiO₂ film resembles approximately the measured spectrum (red line) as shown in Fig. 5b. The maximum absorption is about 90% near 650 nm, and a shallow dip occurs near 500 nm. As for the various values of TiO₂ thickness, including 5, 10, 20, 30, and 50 nm, the absorption spectra of the absorbers are presented in Fig. S4, which coincide with the experimental results in Fig. 3d. The optimal absorption occurs at the thickness of 30 nm. To further understand the optical property of the 30-nm TiO₂-Au bilayer, the electric field distributions are also simulated in some transverse cross-sections. The position *Z* of the cross-section is defined using the vertical displacement from the upper surface of the flat Au layer. The electric field distributions for cross-sections at *Z* = 0, 30, 60, and 90 nm are depicted in Fig. 5c–f, respectively. It can be seen that some hot spots occur near the sites of the particles, indicating the LSPR effect and the plasmonic coupling effect. These effects play a central role in the overall enhancement of absorption. For the broadband absorption, the shell layer and the flat layer of TiO₂ can be regarded as the effective index media for index matching. The TiO₂ layer also modifies the coupling between the Au NPs, which can be used to tailor the absorption in the visible light band.

Discussions

Mechanism of photocurrent generation. For effective generation of photocurrent, the optical absorption is only the first step. As mentioned above, the enhancement of optical absorption is due to the LSPR effect and the plasmonic coupling of the random Au nanostructures in the rough Au film^{5,30–32}. The next step to the photocurrent generation relies on the excitation, separation and transfer of charge carriers. Figure 6 depicts the two mechanisms of the photocurrent generation in the TiO₂-Au bilayer: *hot electron injection* (HEI) and *plasmonic resonance energy transfer* (PRET). Both mechanisms are widely used for the plasmonic enhancement of photocurrent in literature^{2,5,6,17,18,27}. The HEI is illustrated in Fig. 6a, the light incident on the sample excites the plasmonic resonance of electrons in the Au nanostructures, part of these plasmons decays into hot electrons, which are then fed into the conduction band of TiO₂. This enables the creation of active electrons in the TiO₂ nanoparticles even in the absence of direct light absorption by TiO₂^{33,34}. As the rough Au film of the TiO₂-Au bilayer enables the plasmons at different wavelengths, hot electrons of different energies may be excited and injected to the TiO₂ conduction band. In contrast, the PRET goes through a different way as shown in Fig. 6b. The plasmonically excited electrons in the Au film do not migrate into the TiO₂ film, instead they can transfer the energy to the valence-band electrons of TiO₂ film to excite them to the conduction band of TiO₂. This energy transfer process can be enabled by the intense electric field of plasmonic resonance. More specifically, the incident photons excite the collective oscillation of the electrons in Au nanostructures, and thus generate intense oscillating electric fields nearby the Au surface. The region with intense electric field is often called hot spot. The hot

spots can penetrate into the TiO₂ film (typically by a distance of ~10 nm) and thus the oscillating electric fields can excite the TiO₂ electrons. The HEI and the PRET have different requirements. The former needs the Au nanostructures to be directly in physical contact with the TiO₂ for hot electron transfer and also the photon energy to be high enough to overcome the potential barrier at the Au/TiO₂ interface, which has a barrier height of about ~1 eV. The latter requires the overlapping of the absorption spectra of the Au nanostructure and the TiO₂ film, and needs also the extension of the hot spot into the TiO₂ film. Fortunately, all of these conditions are satisfied in our TiO₂-Au bilayer. For example, the rough Au surface is directly covered by the TiO₂ film, and thus the direct electron transfer is enabled and the hot spots can cover part of the TiO₂ film near the rough Au surface; over the strong absorption band of 400–800 nm of the TiO₂-Au bilayer (see Fig. 1b), the corresponding photons energy is in the range of 3.1–1.55 eV, sufficiently higher than the potential barrier ~1 eV; in addition, the TiO₂ film has certain absorption over 400–700 nm (see Fig. 1b) due to the defects in the TiO₂ film whereas the rough Au film itself has flat absorption over 400–800 nm (see Fig. S2e), enabling the overlapping of the absorption spectra. Based on these, we attribute to both the HEI and the PRET for the photocurrent enhancement.

For the influence of the TiO₂ film thickness on the photocurrent of the TiO₂-Au bilayer structure, the TiO₂ film serves three functions. First, the TiO₂ film is a dielectric layer and acts as the index matching layer and assists the optical coupling of the incident light into the rough Au film¹⁸. Thicker or thinner TiO₂ film would deteriorate the effects of index matching and optical coupling. As a result, there is an optimal TiO₂ thickness for optical coupling. Second, the ALD-deposited and thermally-annealed TiO₂ film has more defects and causes additional energy states inside the TiO₂ bandgap, enabling to absorb visible light. Since the defects and the associated energy states vary with the TiO₂ thickness, the absorption of visible light is changed. Third, the TiO₂ film of the TiO₂-Au bilayer provides an electron receptor and also an diffusion layer for the transport of the hot electrons to the TiO₂/solution interface for photochemical reactions^{35,36}. Thin TiO₂ film causes low volume to receive electrons but enables fast transport of electrons due to the short diffusion length, whereas thick TiO₂ film benefits the electron reception but impairs the electron transport due to the long diffusion length. The combined effect of the optical coupling, the defect-induced visible absorption and the electron reception/transport results in the existence of an optimal thickness of TiO₂ film, which happens to be 30 nm in this work. This is the reason that the TiO₂-Au bilayer yields the highest photocurrent when the TiO₂ film is 30 nm thick, as shown in Fig. 4b. As a consequence, the optimal efficiency of photocurrent generation is achieved when the TiO₂-Au bilayer sample has the 30-nm-thick TiO₂ film.

In conclusion, we have examined the rough Au film to sensitize TiO₂ to visible light over 400–800 nm. Burying the rough Au film under the TiO₂ film forms the TiO₂-Au bilayer and induces the broadband optical absorption and the significant enhancement of photocurrent as compared to the other two types of control samples, the TiO₂-AuNP hybrid and the bare TiO₂ film. Such enhancement is ascribed to the LSPR and coupling effects of the random Au nanostructures in the rough Au film for the strong visible absorption and to also the Schottky junction in the Au/TiO₂ interface for the separation of photogenerated electrons and holes. Besides, the optimal thickness of TiO₂ film for the TiO₂-Au bilayer is found to be 30 nm. The superior optical and photoelectrochemical properties of the TiO₂-Au bilayer demonstrate its great potential as the photoelectrode for future environmental and energy technologies. Moreover, this new photoelectrode possesses the merits of high absorption efficiency, broadband absorption of visible light, low production cost and easy fabrication process, and brings new insight into the design and preparation of advanced visible-light responsive photocatalytic materials.

Methods

Preparation of rough Au films, Au nanoparticles and TiO₂ films. Deposition of rough Au film on the FTO glass is performed in a magnetron sputtering system that is equipped with three cathodes in a pure Ar atmosphere at 6×10^{-3} Pa. Before deposition, the FTO glass with a size of $10 \times 10 \times 2$ mm³ is rinsed successively with acetone and methanol in an ultrasonic bath for 10 min, and then dried with a pure nitrogen flow. The separation distance between the target and the substrate is maintained at 10 cm throughout the deposition, while the substrate speed is set at 6 rpm. For the formation of rough Au films, a thin Cr film is first deposited on the FTO as an adhesion layer, and a 100 nm-thick Au film is then deposited by the sputtering method. For the fabrication of Au NPs, a thin Au film of about 8 nm thick is deposited on the FTO glass, which is transformed into Au NPs after the annealing process at 500 °C for 1 h in a furnace. Among various preparation methods of Au NPs, this physical sputtering method is simple, low cost, and easy to fabricate diverse composite films with uniformly distributed metal particles^{37,38}.

The TiO₂ film is deposited onto three different substrates, including the Au film, the Au NPs and the FTO glass slide, respectively, using a commercial atomic laser deposition (ALD) reactor (Cambridge NanoTech, G2 Savannah). Correspondingly, three types of samples, the TiO₂-Au bilayer, the TiO₂-AuNP hybrid and the bare TiO₂ film, are obtained as shown in Fig. 1a. The ALD procedure involves an alternating exposure of Tetrakis dimethylamido titanium (TDMAT), Ti(NMe₂)₄ and deionized water vapor as the precursor carriers at a process temperature of 100 °C with N₂, and then the purge gas at a pressure of 90 sccm. Both the pulse time and the purge time for the precursors are 2 s. The deposition rate of TiO₂ is estimated to be 0.55 Å per cycle. The thickness of TiO₂ film is tuned by controlling the deposition time. After the ALD deposition, the TiO₂ films are annealed at 500 °C for 1 h. To study the influence of TiO₂ thickness, TiO₂ films with a series of thicknesses (i.e., 5, 10, 20, 30 and 50 nm) are deposited on the 30-nm-thick Au film to obtain five samples of the TiO₂-Au bilayer.

Characterization of bilayer structures. The morphology and the particle size of the samples, including the Au film, the Au NPs and the TiO₂ film, are observed by scanning electron microscope (SEM, JEOL Model JSM-6490). The surface morphology and the height information of the Au film are also obtained by atomic force microscope (AFM, Veeco Nanoscope V). The X-ray diffraction (XRD) pattern is recorded using a X-ray

diffractometer (Rigaku SmartLab). The TiO₂ films with different thicknesses on the Au film are recorded using the Cu K_α radiation and the scanning speed of 5°/min with the 2θ range from 10 to 80°.

Optical and photoelectrochemical measurements. The optical reflection and transmission spectra of the TiO₂-Au bilayer, the TiO₂-AuNP hybrid and the bare TiO₂ film are recorded over a wavelength range of 400–800 nm using a UV-Vis spectrophotometer (Shimadzu, UV-2550). Reflection measurements are performed with an integrating sphere that uses a BaSO₄ plate as the reference. This means that both the direct reflected light and the diffuse scattering light are included in the reflection measurement. The photocatalytic reaction and the IPCE action spectra are measured with an electrochemical workstation (CH Instruments, CHI 660E) in a standard three-electrode configuration. To obtain the IPCE action spectra, band-pass filters with a bandwidth less than 15 nm full-width at half-maximum (FWHM) are used. The TiO₂-Au bilayer, the TiO₂-AuNP hybrid and the bare TiO₂ film are used as the working electrode, respectively. A Pt wire electrode is used as the counter electrode and a saturated calomel electrode (SCE) as the reference electrode. Besides, KOH aqueous solution (1 M) is used as the electrolyte. The working electrode is illuminated over an area of about 1 cm² under a simulated solar source (AM 1.5 G, 300 mW/cm²) with a UV-cutoff filter to obtain visible light with $\lambda \geq 400$ nm.

Simulation. A commercial FDTD software (Lumerical FDTD Solutions) is implemented to conduct all the optical simulations. A 3D simulation model is built up according to the physical structure, the material, and the fabrication process of the actual samples.

References

- Khan, S. U. M., Al-Shahry, M. & Ingler, W. B. Efficient photochemical water splitting by a chemically modified n-TiO₂. *Science* **297**, 2243–2245 (2002).
- Warren, S. C. & Thimsen, E. Plasmonic solar water splitting. *Energy Environ. Sci.* **5**, 5133–5146 (2012).
- Fujishima, A., Rao, T. N. & Tryk, D. a. Titanium dioxide photocatalysis. *J. Photochem. Photobiol. C Photochem. Rev.* **1**, 1–21 (2000).
- Umebayashi, T., Yamaki, T., Tanaka, S. & Asai, K. Visible light-induced degradation of methylene blue on S-doped TiO₂. *Chem. Lett.* **32**, 330–331 (2003).
- Zhang, X., Chen, Y. L., Liu, R.-S. & Tsai, D. P. Plasmonic photocatalysis. *Rep. Prog. Phys.* **76**, 046401 (2013).
- Furube, A., Du, L., Hara, K., Katoh, R. & Tachiya, M. Ultrafast plasmon-induced electron transfer from gold nanodots into TiO₂ nanoparticles. *J. Am. Chem. Soc.* **129**, 14852–14853 (2007).
- Mock, J. J., Barbic, M., Smith, D. R., Schultz, D. a. & Schultz, S. Shape effects in plasmon resonance of individual colloidal silver nanoparticles. *J. Chem. Phys.* **116**, 6755 (2002).
- Huang, X., El-sayed, I. H., Qian, W. & El-sayed, M. A. Cancer cell imaging and photothermal therapy in the near-infrared region by using gold nanorods. *J. Am. Chem. Soc.* **128**, 2115–2120 (2006).
- Heo, C.-J., Kim, S.-H., Jang, S. G., Lee, S. Y. & Yang, S.-M. Gold ‘Nanograins’ with tunable dipolar multiple plasmon resonances. *Adv. Mater.* **21**, 1726–1731 (2009).
- Kochuveedu, S., Kim, D. & Kim, D. Surface-plasmon-induced visible light photocatalytic activity of TiO₂ nanospheres decorated by Au nanoparticles with controlled configuration. *J. Phys. Chem. C* **116**, 2500–2506 (2012).
- Gole, J. L., Stout, J. D., Burda, C., Lou, Y. & Chen, X. Highly efficient formation of visible light tunable TiO_{2-x}N_x photocatalysts and their transformation at the nanoscale. *J. Phys. Chem. B* **108**, 1230–1240 (2004).
- Hsu, C. Y. *et al.* Supersensitive, ultrafast, and broad-band light-harvesting scheme employing carbon nanotube/TiO₂ core-shell nanowire geometry. *ACS nano* **6**, 6687–6692 (2012).
- Naldoni, A. *et al.* Effect of nature and location of defects on bandgap narrowing in black TiO₂ nanoparticles. *J. Am. Chem. Soc.* **134**, 7600–7603 (2012).
- Kravets, V. G., Neubeck, S., Grigorenko, a. N. & Kravets, a. F. Plasmonic blackbody: Strong absorption of light by metal nanoparticles embedded in a dielectric matrix. *Phys. Rev. B - Condens. Matter Mater. Phys.* **81**, 1–9 (2010).
- Buso, D., Pacifico, J., Martucci, A. & Mulvaney, P. Gold-nanoparticle-doped TiO₂ semiconductor thin films: Optical characterization. *Adv. Funct. Mater.* **17**, 347–354 (2007).
- Connelly, K., Wahab, a. K. & Idriss, H. Photoreaction of Au/TiO₂ for hydrogen production from renewables: a review on the synergistic effect between anatase and rutile phases of TiO₂. *Mater. Renew. and Sustain. Energy* **1**, 3 (2012).
- Wu, X. *et al.* Broadband plasmon photocurrent generation from Au nanoparticles/mesoporous TiO₂ nanotube electrodes. *Solar Energy Mater. Solar Cells* **138**, 80–85 (2015).
- Shi, X., Ueno, K., Oshikiri, T. & Misawa, H. Improvement of plasmon-enhanced photocurrent generation by interference of TiO₂ thin film. *J. Phys. Chem. C* **117**, 24733–24739 (2013).
- Hou, Y., Li, X., Zhao, Q., Quan, X. & Chen, G. TiO₂ nanotube/Ag–AgBr three-component nanojunction for efficient photoconversion. *J. Mater. Chem.* **21**, 18067 (2011).
- White, J. R. Annealing behaviour of thin evaporated gold films. *Thin Solid Film* **22**, 23–35 (1974).
- Gupta, G. *et al.* Absorption spectroscopy of gold nanoisland films: Optical and structural characterization. *Nanotechnology* **20**, 025703 (2009).
- Cheng, H.-E. & Chen, C.-C. Morphological and photoelectrochemical properties of ALD TiO₂ films. *J. Electrochem. Soc.* **155**, D604 (2008).
- King, D. M., Du, X., Cavanagh, A. S. & Weimer, A. W. Quantum confinement in amorphous TiO₂ films studied via atomic layer deposition. *Nanotechnology* **19**, 445401 (2008).
- Chen, Z. *et al.* Inverse opal structured Ag/TiO₂ plasmonic photocatalyst prepared by pulsed current deposition and its enhanced visible light photocatalytic activity. *J. Mater. Chem. A* **2**, 824 (2014).
- Liu, L., Zhao, H., Andino, J. M. & Li, Y. Photocatalytic CO₂ reduction with H₂O on TiO₂ nanocrystals: Comparison of anatase, rutile, and brookite polymorphs and exploration of surface chemistry. *ACS Catal.* **2**, 1817–1828 (2012).
- Temnov, V. V. *et al.* Active magneto-plasmonics in hybrid metal–ferromagnet structures. *Nat. Photonics* **4**, 107–111 (2010).
- Ingram, D. B. & Linic, S. Water splitting on composite plasmonic-metal/semiconductor photoelectrodes: Evidence for selective plasmon-induced formation of charge carriers near the semiconductor surface. *J. Am. Chem. Soc.* **133**, 5202–5205 (2011).
- Cao, S. *et al.* Hierarchic random nanosphere model for broadband solar energy absorbers. *Opt. Mater. Express* **5**, 2777 (2015).
- Chan, S.-H. *et al.* Controllable photonic mirror fabricated by the atomic layer deposition on the nanosphere template. *Appl. Opt.* **53**, A237–A241 (2014).
- Zhang, N. *et al.* Ultrabroadband metasurface for efficient light trapping and localization: A universal surface-enhanced Raman spectroscopy substrate for ‘All’ excitation wavelengths. *Adv. Mater. Interfaces* **2**, 1500142 (2015).
- Wang, H. U. I. & Brandl, D. W. Plasmonic Nanostructures: Artificial molecules nanoshell plasmons: the Sphere-Cavity. *Acc. Chem. Res.* **40**, 53–62 (2007).

32. Liu, Z. *et al.* Automatically acquired broadband plasmonic-metamaterial black absorber during the metallic film-formation. *ACS Appl. Mater. Interfaces* **7**, 4962–4968 (2015).
33. Tian, Y. & Tatsuma, T. Mechanisms and applications of plasmon-induced charge separation at TiO₂ films loaded with gold nanoparticles. *J. Am. Chem. Soc.* **127**, 7632–7637 (2005).
34. Liu, E. *et al.* A facile strategy to fabricate plasmonic Au/TiO₂ nano-grass films with overlapping visible light-harvesting structures for H₂ production from water. *J. Mater. Sci.* **50**, 2298–2305 (2014).
35. Mora-Seró, I. *et al.* Photosensitization of TiO₂ layers with CdSe quantum dots: Correlation between light absorption and photoinjection. *J. Phys. Chem. C* **111**, 14889–14892 (2007).
36. Baglio, V., Girolamo, M., Antonucci, V. & Aricò, a S. Influence of TiO₂ film thickness on the electrochemical behaviour of dye-sensitized solar cells. *Int. J. Electrochem. Sci* **6**, 3375–3384 (2011).
37. Lee, K.-C., Lin, S.-J., Lin, C.-H., Tsai, C.-S. & Lu, Y.-J. Size effect of Ag nanoparticles on surface plasmon resonance. *Surf. Coatings Technol.* **202**, 5339–5342 (2008).
38. Nazirzadeh, M. A., Atar, F. B., Turgut, B. B. & Okyay, A. K. Random sized plasmonic nanoantennas on silicon for low-cost broadband near-infrared photodetection. *Sci. Rep.* **4**, 7103 (2014).

Acknowledgements

This work is supported by National Science Foundation of China (no. 61377068), Research Grants Council (RGC) of Hong Kong (N_PolyU505/13, PolyU 5334/12E, and PolyU 152184/15E), and The Hong Kong Polytechnic University (G-YN07, G-YBBE, 4-BCAL, 1-ZVAW, 1-ZE14, A-PM21, 1-ZE27 and 1-ZVGH).

Author Contributions

F.T. proposed the whole research direction and guided the project. T.L. designed and performed the simulation. F.T. and X.Z. wrote and revised the manuscript. N.W., S.K.L., C.S.T. and W.Y. helped with experiment.

Additional Information

Supplementary information accompanies this paper at <http://www.nature.com/srep>

Competing financial interests: The authors declare no competing financial interests.

How to cite this article: Tan, F. *et al.* Rough gold films as broadband absorbers for plasmonic enhancement of TiO₂ photocurrent over 400–800 nm. *Sci. Rep.* **6**, 33049; doi: 10.1038/srep33049 (2016).



This work is licensed under a Creative Commons Attribution 4.0 International License. The images or other third party material in this article are included in the article's Creative Commons license, unless indicated otherwise in the credit line; if the material is not included under the Creative Commons license, users will need to obtain permission from the license holder to reproduce the material. To view a copy of this license, visit <http://creativecommons.org/licenses/by/4.0/>

© The Author(s) 2016